Supplementary Information (SI) for Inorganic Chemistry Frontiers.

SUPPORTING INFORMATION

Aqueous phase synthesis and electronic spectroscopy of nanostructured layered double hydroxides

Marco Piccinni[1], Christian Rossi[1], Diego Colombara*[1,2], Francesco Bonaccorso*[2,3]

[1] Dipartimento di Chimica e Chimica Industriale, Università degli Studi di Genova, via Dodecaneso 31, 16146 Genoa, Italy.
[2] Istituto Italiano di Tecnologia, via Morego 30, Genoa, Italy.
[3] BeDimensional Spa., via Lungotorrente Secca 30R, 16163 Genoa, Italy.

* Email: diego.colombara@unige.it
* Email: francesco.bonaccorso@iit.it

DC and CR acknowledge the Italian Ministry of University and Research for funding through the LEGACY (healing wide-gap chalcopyrite, grant No. 20223ZP4WP) project of national relevance (PRIN 2022), under the ERC PE3 Condensed Matter Physics sector.

Table of Contents

1. Chemicals

Aluminium nitrate nonahydrate ($Al(NO_3)_3 \cdot 9H_2O$, ACS reagent, ≥98%), ethanol ($EtOH$, puriss. p.a., absolute, ≥99.8% (GC)), ferric nitrate nonahydrate ($Fe(NO_3)_3 \cdot 9H_2O$, ACS reagent, ≥98%), nickel acetate tetrahydrate ($Ni(AcO)_2 \cdot 4H_2O$, purum p.a., ≥99.0% (KT)), nickel nitrate hexahydrate ($Ni(NO_3)_2 \cdot 6H_2O$, puriss. p.a., ≥98.5% (KT)), urea ($OC(NH_2)_2$, ACS reagent, 99.0-100.5%), triethanolamine ($N(CH_2CH_2OH)_3$, ≥99.0% (GC)), trisodium citrate dihydrate ($Na_3C_6H_5O_7 \cdot 2H_2O$, meets USP testing specifications), sodium hydroxide ($NaOH$, reagent grade, ≥98%, pellets (anhydrous)), and zinc nitrate hexahydrate ($Zn(NO_3)_2 \cdot 6H_2O$, purum p.a., crystallized, ≥99.0% (KT)) were purchased from Sigma-Aldrich and used without further purification. Unless otherwise specified, we used as solvent deionized water previously degassed by boiling it for 20 min under Ar bubbling (Air Liquide), to avoid atmospheric CO_2 contamination.

2. Synthesis of citrate-intercalated LDHs

Table S1 reports the procedures that we optimized for the synthesis of citrate intercalated LDHs by hydrolytic polymerization. Different synthetic conditions are required for the synthesis of pure ZnAl-LDH, as displayed in **Figure S2b**. As discussed in the main article the ZnAl system has a different hydrolytic behaviour compared to the Ni-based ones. The synthesis of ZnFe-LDH is not reported since is not possible from Fe^{3+} precursors[1].

Table S1. *Synthetic details of citrate-intercalated NiAl-, NiFe- and ZnAl-LDHs.*

Step	NiAl- or NiFe-LDH	ZnAl-LDH
1)	0.4 mmol of $Al(NO_3)_3 \cdot 9H_2O$ (*i.e.*, 150.0 mg) or $Fe(NO_3)_3 \cdot 9H_2O$ (*i.e.*, 161.6 mg) are dissolved into 160 mL of water alongside 1.2 mmol of $Ni(AcO)_2 \cdot 4H_2O$ (*i.e.*, 298.6 mg) in a 250 mL glass bottle.	6 mmol of $Al(NO_3)_3 \cdot 9H_2O$ (*i.e.*, 2.25 g) are dissolved into 160 mL of water alongside 12 mmol of $Zn(NO_3)_2 \cdot 6H_2O$ (*i.e.*, 3.57 g) in a 250 mL glass bottle.
2)	1.6 mmol of $Na_3C_6H_5O_7 \cdot 2H_2O$ (*i.e.*, 470.6 mg) are dissolved into 4 mL of water and then added to the solution prepared in step 1) under vigorous stirring. The bottle is sealed and heated on a hot plate set at 80°C under stirring. After one hour, the bottle is let to cool down to ambient temperature.	18 mmol of $Na_3C_6H_5O_7 \cdot 2H_2O$ (*i.e.*, 5.29 g) are dissolved into 10 mL of water and then added to the solution prepared in step 1) under vigorous stirring. The bottle is sealed and heated on a hot plate set at 80°C under stirring. After one hour, the bottle is let to cool down to ambient temperature.
3)	30 mL of a $NaOH$ 0.1 M solution is added dropwise to the step 2) solution under vigorous stirring.	34 mL of a $NaOH$ 1 M solution is added dropwise to the step 2) solution under vigorous stirring.
4)	The step 3) solution is transferred into a three-neck 250 mL round flask and heated to 90°C by using a heating mantle. The temperature is measured by placing a thermometer in direct contact with the solution. The flask is connected to a bubble condenser to avoid water evaporation and the whole apparatus is kept filled with Ar to avoid atmospheric CO_2 contamination.	The step 3) solution is transferred into a three-neck 250 mL round flask and heated to 60°C by using a heating mantle. The temperature is measured by placing a thermometer in direct contact with the solution. The flask is connected to a bubble condenser to avoid water evaporation and the whole apparatus is kept filled with Ar to avoid atmospheric CO_2 contamination.
5)	After three days, the product of step 4) is collected by centrifugation at 3000 relative centrifugal force and washed three times with 10 mL of water.	After three days, the product of step 4) is collected by centrifugation at 3000 relative centrifugal force and washed three times with 10 mL of water.

Citrate-intercalated LDHs are stored as powders obtained by freeze-drying the precipitates from step 5) at -50°C for two days.

The freeze-dried LDH powders should be handled with care since the risk to inhale them is real. We always handled LDH powders under fume hood while wearing FFP2 face masks. Then, all surfaces that may be exposed to LDH powders are cleaned with water.

The synthesis of LDHs with different metal ratio is achieved by changing the molar ration of metal precursors in Step 1, but by keeping the overall metal concentration unaltered.

We also synthetized carbonate-intercalated NiFe-LDH as a reference material by homogeneous precipitation from a solution containing both metal nitrate salts, triethanolamine and urea, following the same procedure described in literature by S. Jaśkaniec et al.[2]. Briefly 1.2 mmol of $Ni(NO_3)_2 \cdot 6H_2O$ (349 mg), 0.4 mmol of $Fe(NO_3)_3 \cdot 9H_2O$ (161.6 mg) and 2.8 mmol of urea (168.2 mg) are dissolved in water up to a volume of 160 ml. The solution is transferred to a glass bottle and 1.6 mmol of triethanolamine (212.4 µL) are added dropwise under vigorous stirring, then the bottle is sealed and left under stirring for 24h at ambient temperature. Subsequently, as described by Jaśkaniec et al. [2], a ferrihydrite ($FeOOH \cdot xH_2O$) suspension forms. This suspension is transferred in a 250 ml round flask and heated at 100°C under reflux for 48h. Degassing water is

not necessary for this synthesis. The obtained product, carbonate-intercalated NiFe-LDH, was then isolated by centrifugation at 3000 relative centrifugal force and washed three times by replacing the supernatant with 10 mL of water.

3. Composition

Metal ratios in LDH materials were analysed by X-ray fluorescence (XRF) with a Bruker M4 TORNADO Micro X-ray Fluorescence. The samples for XRF analysis were prepared by compressing the LDH powder into a pellet with 4 mm diameter and ~1 mm thickness. The atomic metal percentage (% At.) values are the result of the average on three different sampling points, see **Table S2**.

Table S2. *Atomic percent composition (% At.) of citrate intercalated LDHs.*

Sample	M^{2+} (% At.)	M^{3+} (% At.)
NiAl-LDH	85.71	14.22[a]
NiFe-LDH	73.50	26.50
ZnAl-LDH	84.86	15.14

[a] A 0.07% At. contamination by Fe has been detected. This contamination probably originates from the usage of technical-grade reagents.

4. Morphology and crystal structure

Transmission electron spectroscopy (TEM) images were acquired with a JOEL JEM-1011 - 100 kV TEM (W filament thermionic source). High resolution TEM (HRTEM) images were acquired with a JOEL JEM-2100plus - 200 kV HRTEM. The samples for the TEM and HRTEM measurements were prepared by drop casting 5 µL of diluted LDH dispersions in ethanol (~1 µg/mL) onto ultrathin C-on-holey Cu grids (TED PELLA Inc.).

Scanning electron microscope (SEM) images where acquired with Zeiss Evo 40 (Carl Zeiss SMT Ltd, Cambridge, England).

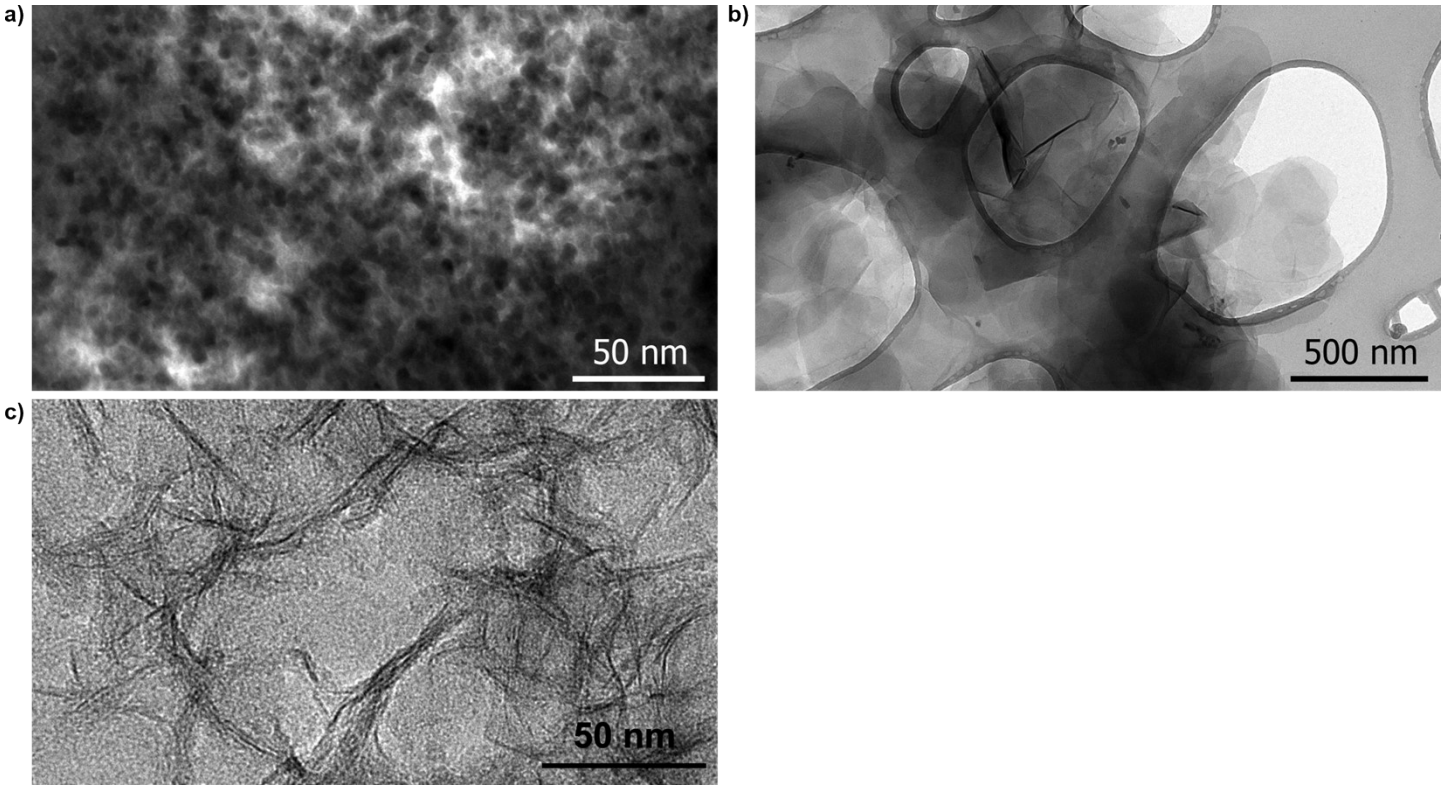

Figure S1. *Transmission electron microscopy images of a) citrate-intercalated NiAl-LDH nanosheets and b) citrate-intercalated ZnAl-LDH nanosheets c) HRTEM image of NiFe-LDH aggregates.*

X-ray diffraction (XRD) measurements were acquired with a Malvern PANalytical Empyrean X-ray diffractometer operating at 1.8 kW with a Cu Kα X-ray tube. We intentionally did not perform any data treatment on the XRD patterns (*i.e.*, background subtraction, smoothing) to avoid the accidental creation of artifacts. The unit cell a and c axis reported in **Table 1** in the main article have been estimated from the scattering angle (2θ) position of reflections in the LDHs diffraction pattern as follows for a lattice of the hexagonal crystal family ($a = b \neq c$, $\alpha = \beta = 90°$, $\gamma = 120°$):

$$d_{hkl} = \frac{1}{(h^2 + k^2 + hk)a^{*2} + l^2 c^{*2}} .\#(S1)$$

Where a^* and c^* are the reciprocal lattice dimensions, which are defined as:

$$a^* = \frac{2}{a\sqrt{3}},\ c^* = \frac{1}{c} .\#(S2)$$

While d_{hkl} are the lattice parameters calculated according to Bragg's law as follows:

$$2d_{hkl}\sin(\theta) = n\lambda_{x\text{-}rays} .\#(S3)$$

Then, unit cell axes are calculated by the following relationships:

$$a = 2 \cdot d_{110} \#(S4)$$

$$c = \frac{1}{n}\sum_{i=1}^{n} l_i \cdot (d_{00l})_i \#(S5)$$

For a straightforward comparison, our results are reported alongside other citrate intercalated LDHs and LDH minerals in **Table S3**.

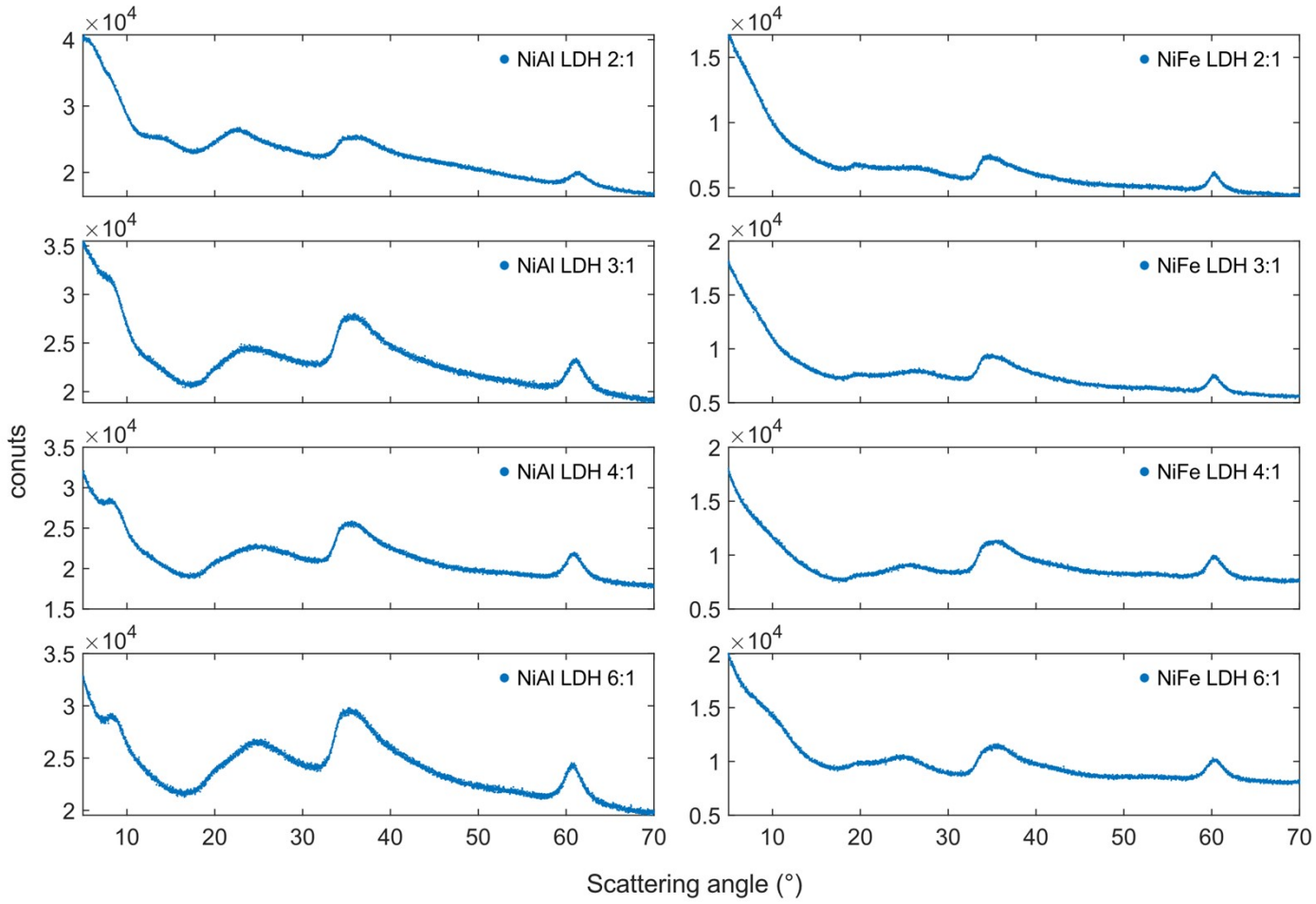

Figure S2. *Powder X-ray diffraction patterns of citrate intercalated LDHs with variable metal ratio.*

4.1. Comparative table of crystallographic parameters

Table S3. *Crystallographic parameters of natural and synthetic LDHs.*

Synthetic LDHs

M^{2+}	M^{3+}	A^{n-}	Basal spacing (nm)	a-axis (nm)	c-axis (nm)	Reference
Ni	Al	Citrate	1.223	0.3019	3.669	This work
Ni	Fe	Citrate	1.227	0.3053	3.680	This work
Zn	Al	Citrate	1.222	0.3056	3.665	This work
Ni	Fe	Carbonate	0.770	n.a.	n.a.	[3]
Ni	Fe	Carbonate	0.784	n.a.	n.a.	[3]
Ni	Fe	Citrate	1.22	n.a.	n.a.	[3]
Mg	Al	Citrate	1.20	n.a.	n.a.	[4]
Mg	Al	Citrate	1.18	n.a.	n.a.	[5]
Ni	Al	Citrate	1.17	n.a.	n.a.	[5]
Zn	Al	Citrate	1.23	n.a.	n.a.	[5]
Zn	Al	Citrate	1.22	n.a.	n.a.	[6]
Zn	Al	Nitrate	0.89	0.308	n.a.	[6]
Ni	Al	Carbonate	0.7513	0.3023	2.2538	[7]
Ni	Fe	Carbonate	0.7481	0.3070	2.2443	[7]
Ni	Fe	Carbonate	0.7596	0.3080	2.2789	[7]
Ni	Al	Nitrate	0.860	0.300	2.58	[8]
Ni	Fe	Nitrate	0.794	0.307	2.382	[8]
Ni	Fe	Adipate	1.308	0.307	3.925	[8]
Ni	Fe	Sebacate	1.539	0.307	4.617	[8]

LDH minerals[a]

Mineral name: composition	Basal spacing (nm)	a-axis (nm)	c-axis (nm)	Reference
Hydrotalcite: $Mg_6Al_2(OH)_{16}CO_3 \cdot 4H_2O$	n.a.	0.3065	2.307	[9]
Takovite: $Ni_6Al_2(OH)_{16}CO_3 \cdot 4H_2O$	n.a.	0.30250	2.2595	[9]
Reevesite: $Ni_6Fe_2(OH)_{16}CO_3 \cdot 4H_2O$	n.a.	0.3082	2.2770	[9]
Zaccagnaite: $Zn_4Al_2(OH)_{12}CO_3 \cdot 4H_2O$	n.a.	0.30662	2.26164	[9]

[a] All LDH minerals are referred to 3R polymorphs. Despite for 3R LDH polymorphs the unit cell c axis and the basal plane are in a 3:1 relationship, we decided to only include what is actually reported in referenced works.
n.a. = not available.

5. Potentiometric titrations

Potentiometric titrations were carried out in our custom setup under continuous argon flow. Titrations are carried out in 150 ml RDE/RRDE jacketed cell (Pine Research Instrumentation, Inc.). The temperature is controlled at 25.0±0.1 °C with a MAGIO MS-1000F thermo-cryostat (JULABO Italia S.r.l.) connected to the jacket of the titration cell. pH measurements were sampled every 15 s with a pH-meter XS pH 8 PRO (GIORGIO BROMAC S.r.l.), sent to the interfaced PC via USB and recorded by the pH-meter own software. The pH-meter is equipped with an XS Sensor Polymer HA PRO (GIORGIO BROMAC S.r.l.) for pH measurement and an NT 55 thermometer (GIORGIO BROMAC S.r.l.) for automatic temperature compensation. Titrant solutions were prepared in volumetric flasks (Scharlab Italia S.r.l.) and injected by a NE-4000 Double Syringe Pump (KF Technology) equipped with one 19.95 mm diameter syringe. The titrant flow rate is set to 10.00 ml/h. Before measurements the pH-meter is calibrated with a 4.01/7.00/10.01 pH buffer calibration set (GIORGIO BROMAC S.r.l.). The differential titration profiles are computed from digitalized titration data with MATLAB R2021b software using a five-points lowess smoothing algorithm as noise filtering function.

The speciation diagrams are computed with HySS software[10] in the desired pH range starting from literature data. In details, HySS calculates the concentration of the free reagents by solving the mass-balance equation considering the stoichiometric coefficients of the species, their concentration, and the equilibria in the system. The corresponding equilibrium constants were critically selected from NIST database[11] and relevant papers[12–18]. Generally, an average value is considered when multiple data is available for the same complex, whereas sometimes the data able to give the better match with experiment was selected. Often the metal-ligand constants ($\log\beta$) reported in the literature needs a rearrangement to meet the requirements of the authors with Hyss software language. For instance, in this work citrate is considered as a tetrabasic ligand, hence $\log\beta$ referring to citrate as tribasic ligand were corrected as follows:

$$\log\beta_{tetrabasic} = \log\beta_{tribasic} + n \cdot pKa_4 .\#(S6)$$

Since the deprotonation of the fourth proton of citrate has a pKa_4= 14.4[19], $(S6)$ becomes:

$$\log\beta_{tetrabasic} = \log\beta_{tribasic} + n \cdot 14.4 ,\#(S7)$$

where n is the number of citrate ligands involved in the complex. A further $\log\beta$ correction is also required by HySS software whenever hydroxide ions are involved in complexes or solid phases. The $\log\beta$ of hydroxide complexes is modified according to the following equation:

$$\log\beta_{HySS} = \log\beta_{literature} - n^{'} \cdot pK_w ,\#(S8)$$

where n' is the number of hydroxide groups involved in the complex and pK_w is the self-dissociation constant of water, *i.e.*, 14.00. Whereas for solid hydroxide phases:

$$\log\beta_{HySS} = - pK_{sp} + n^{''} \cdot pK_w ,\#(S9)$$

where n'' is the number of hydroxides in the solid stoichiometry.

Here a demonstration of $(S6)$ is provided. We define L^* as a generic α-hydroxycarboxylate ligand without considering its hydroxyl group deprotonation. However, such a ligand can form a complex with a metal cation M by deprotonation of its hydroxyl group, as follows:

$$M + nL^* \rightleftharpoons M\left(H_{-1}L^*\right)_n + nH ,\#(S10)$$

with a metal-ligand stability constant expressed as:

$$\beta^* = \frac{\left[M\left(H_{-1}L^*\right)_n\right][H]^n}{[M]\left[L^*\right]^n} .\#(S11)$$

We also define as L the same α-hydroxycarboxylate, but with the hydroxyl group deprotonated. Its related complex formation equilibrium with M is defined as follows:

$$M + nL \rightleftharpoons ML_n ,\#(S12)$$

with a metal-ligand stability constant expressed as:

$$\beta = \frac{[ML_n]}{[M][L]^n}.\#(S13)$$

Now, by considering that $^{H_{-1}L^*} = L$ and $L^* = HL$, the dissociation constant of the hydroxyl group can be defined as:

$$Ka_{OH} = \frac{[H_{-1}L^*][H]}{[L^*]} = \frac{[L][H]}{[HL]}.\#(S14)$$

By algebraic substitution of $(S14)$ into $(S11)$ it follows that:

$$\beta^* = \frac{[ML_n]}{[M][L]^n} \cdot (Ka_{OH})^n,\#(S15)$$

which according to $(S13)$ corresponds to:

$$\beta^* = \beta \cdot (Ka_{OH})^n \#(S16)$$

that in logarithmic form yields:

$$\log \beta = \log \beta^* + n \cdot pKa_{OH}.\#(S17)$$

***Table S4**. Stability constants ($\log \beta$) of complexes and solid phases considered for HySS simulations. Ligands considered: hydroxide (H_{-1}), citrate ($C_5H_4O_7$), acetate ($C_2H_3O_2$).*

Ligand	Species	$\log \beta$	References	Ligand	Species	$\log \beta$	Reference
$L = H_{-1}$*	HL (*i.e.*, H_2O)	-13.77	HySS Default[10]	$L = C_5H_4O_7$	HL	14.40	[19]
	AlL	-5.53	[11]		H_2L	20.80	[19]
	AlL_2	-11.30	[11]		H_3L	25.56	[19]
	AlL_3	-13.50	[11]		H_4L	28.69	[19]
	AlL_4	-23.58	[11]		$AlHL$	22.34	[11]
	Al_2L_2	-7.77	[11]		AlH_2L_2	41.56	[11]
	Al_3L_4	-14.14	[11]		AlH_2L	24.67	[11]
	$Al_{13}L_{32}$	-110.42	[11]		AlH_3L_2	46.16	[18]
	FeL	-3.03	[11]		Al_2L_2	41.49	[11]
	FeL_2	-3.71	[11]		$Al_3L_3H_{-1}$	57.83	[11]
	FeL_3	-11.80	[11]		Al_3HL_3	32.29	[11]
	FeL_3 (s, amorphous)	9.40	[11]		FeL	22.60	[11]
	FeL_4	-21.60	[11]		$FeHL$	25.40	[11,17]
	Fe_2L_2	-3.32	[11]		FeH_2L	27.50	[11]
	Fe_3L_4	-6.13	[11]		FeL_2	32.74	[12]
	NiL	-10.06	[11,13]		$FeHL_2$	38.75	[12]
	NiL_2	-19.50	[11,14]		FeH_2L_2	43.59	[12]
	NiL_2 (s, alpha)	13.60	[11]		Fe_2L_2	50.00	[11]
	NiL_2 (s, alpha)	12.90	[11]		Fe_3L_3	73.80	[12]
	NiL_2 (s, beta)	10.80	[11]		$NiHL$	19.85	[11,13]
	NiL_3	-29.85	[11,15]		NiH_2L	24.18	[11]
	NiL_4	-47.00	[13]		NiH_3L	27.31	[11,13]
	Ni_4L_4	-28.32	[11,13]		NiH_2L_2	37.45	[11,13]
	ZnL	-9.23	[11]		NiH_3L_2	43.08	[11,13]
	ZnL_2	-16.35	[11]		Ni_2L_2	24.66	[11]
	ZnL_2(s, epsilon)	11.90	[11]		$Ni_4L_3H_{-1}$	22.10	[16]
	ZnL_3	-28.40	[11]		$ZnHL$	19.13	[11]
	ZnL_4	-40.90	[11]		ZnH_2L	22.80	[20,21]
	Zn_2L	-8.77	[11]		ZnH_3L	15.60	[11]
	Zn_4L_4	-28.1	[11]		Zn_2L_2**	25.95	[20]
$L = C_2H_3O_2$	HL	4.60	[11]		ZnH_2L_2	35.33	[11]
	NiL	0.91	[11]				
	NiL	1.58	[11]				

* In the HySS software the hydroxide ion is referred to as H_{-1}.

** $Zn_2H_2L_2(H_{-1})_2$. Due to software limitations, HySS cannot distinguish deprotonated alcoholic groups of citrates from coordinated OH.

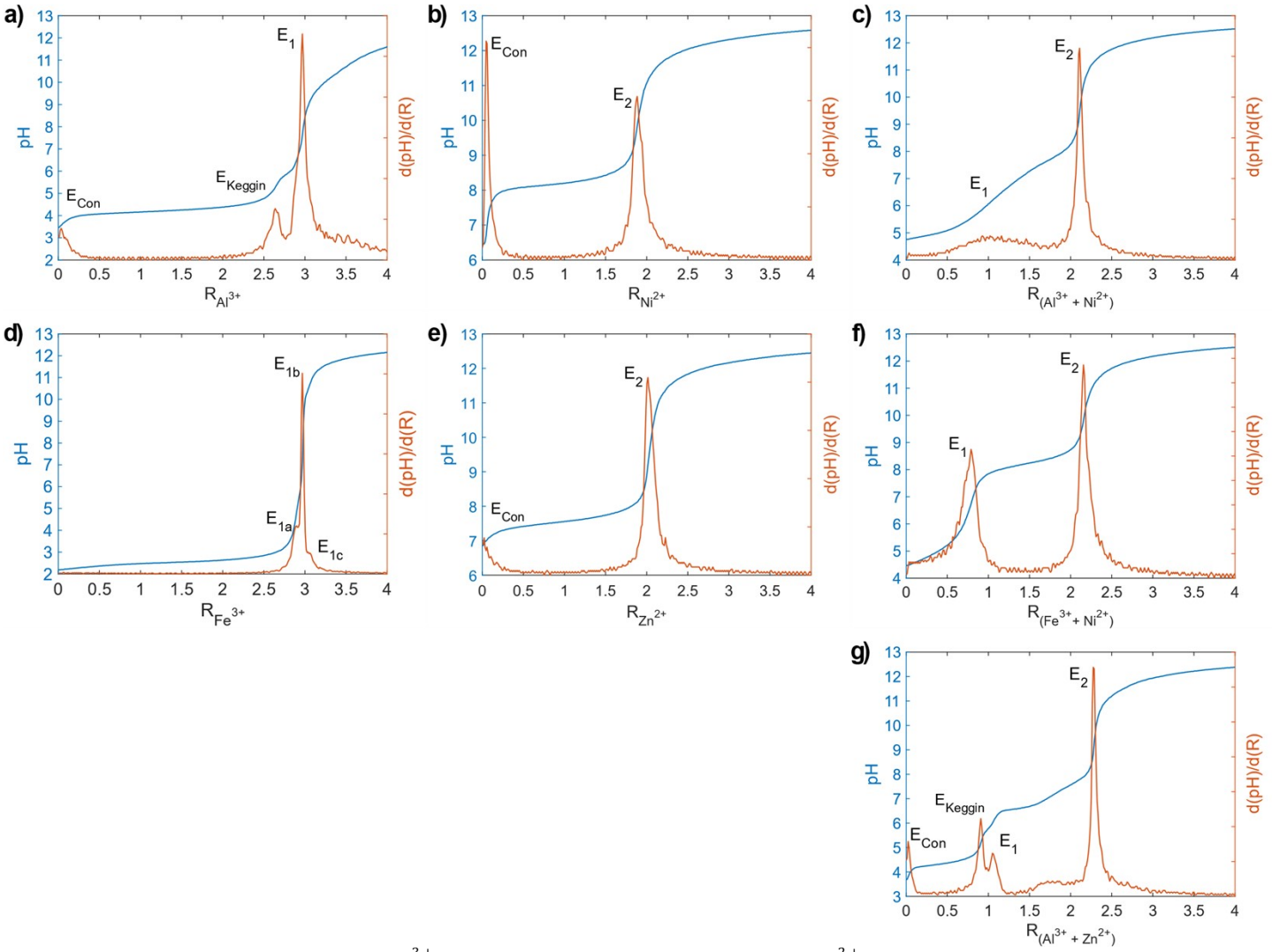

Figure S3. a) Potentiometric titration curves of Fe^{3+} solutions. b) Potentiometric titration curves of Ni^{2+} solutions. c) Comparison between titration curves of M^{2+}-citrate solutions. d) Comparison between titration curves of M^{3+}-citrate solutions.

6. Electronic spectroscopy (UV-Vis-NIR)

Ultraviolet-visible light absorbance spectra were acquired at ambient temperature with a Cary 5000 spectrophotometer from Agilent operating in double beam, baseline-corrected, transmission mode, a wavelength step of 0.5 nm, slit resolution of 0.5 nm and 0.9 s acquisition time for each step. Samples were placed in 1 mL Suprasil® QS quartz cuvettes (Hellma Analytics), setting the optical path to 4 mm. The UV lamp and NIR detector switches were set at 300 and 800 nm, respectively. Solution samples were analysed as prepared, while the carbonate NiFe-LDH reference material was dispersed in ethanol to a concentration of ~0.15 mg/mL before measurements (*cf.* ref. [3]). Absorbance second derivative ultraviolet-visible light spectra were computed with MATLAB R2021b software, using a three-points linear smoothing as noise suppressing function, and applying 10 passes before each differentiation (as described in ref. [3]). Ultraviolet, visible, and near-infrared light reflectance spectra of citrate-intercalated NiAl- and NiFe-LDHs powders were acquired at ambient temperature by equipping the Varian Cary 5000 spectrophotometer with its own integrating sphere accessory operating in total reflectance mode. To acquire reflectance spectra, powder samples were dispersed in water and drop-casted onto circular Suprasil® QX quartz slabs (Hellma Analytics) with 22 mm radius and 2 mm thickness, then they were dried on a hot plate at 100°C. In the measurement setup the quartz slabs were placed on the inner surface of the integrating sphere with a reflector behind them.

6.1. Comparative table of electronic transitions

Table S5. *Absorbance contribution in electronic spectra of natural and synthetic oxides and hydroxides containing Ni and Fe.*

Nickel based LDHs

Sample	Transition wavelength (nm) ν_1	ν_2	ν_3	ν_4	ν_5	ν_6	ν_7	ν_8	ν_9	Ref.
NiFe-LDH	1120	750	665	448	420	386	348[e] 338[f]	250	210	This work
NiAl-LDH	1110	740	655	-	420	383	-	-	210	This work
NiFe-LDH	-	750	650	450	420	385	350	250	210	3
NiFe-LDH	1105	730	630	450	420	375	350	260	210	7
NiAl-LDH	1105	730	630	-	420	375	-	-	210	7
NiAl-LDH	-	730	630	-	420	375	-	-	-	22

Nickel based compounds

Sample	Transitions wavelength (nm) ν_1	ν_2	ν_3	ν_4	ν_5	ν_6	ν_7	ν_8	ν_9	Ref.
Ni:Pyrophyllite	1086	725	649	-		388[b]	-	-	-	23
Exfoliated $Ni(OH)_2$	1100		700[a]	-		400[b]	-	-	-	24
$Ni(OH)_{2-x}(CH_3COO)_x$	1240	761	671	-	440	387[c]	-	-	-	25
β-$Ni(OH)_2$	-		715[a]	-	420	384[c]	-	-	214	26
NiO	-		715[a]	-	429	379[c]	-	-	295	26
β-$Ni(OH)_2$	-		705[a]	-	423	381[c]	-	-	226	27

Iron based compounds

Sample	Transitions wavelength (nm) ν_1	ν_2	ν_3	ν_4	ν_5	ν_6	ν_7	ν_8	ν_9	Ref.
Fe^{3+}:Al_2O_3	-	-	-	449	-	392[d]	373[e] 308[f]	259	194	28
Fe^{3+}:MgO	-	-	-	460	-	398[d]	364[e] 322[f]	279 246[g]	216	28
α-Fe_2O_3	-	-	-	420	-	-	374[e] 314[f]	257	223[g]	28
Nontronite	-	-	-	444	-	384[d]	367[e]	261	200	28
Hematite	-	-	-	444	-	405[d]	380[e] 319[f]	270	-	29
Goethite	-	-	-	435	-	-	365[e] 285[f]	250	225[g]	29
Maghemite	-	-	-	435	-	-	370[e] 315[f]	250	-	29
Lepidocrocite	-	-	-	435	-	-	365[e] 305[f]	239	210[g]	29

[a] The authors reported the average value of ν_2 and ν_3.
[b] The authors reported the average value of ν_5 and ν_6.
[e] *d-d* (Fe^{3+}) $^6A_{1g}(^6S) \rightarrow {}^4E_g(^4D)$ contribution to the absorbance.

[c] *d-d* (Ni^{2+}) $^3A_{2g}(^3F)\rightarrow{}^3T_{1g}(^3P)$ contribution to the absorbance.

[d] *d-d* (Fe^{3+}) $^6A_{1g}(^6S)\rightarrow{}^4T_{2g}(^4D)$ contribution to the absorbance.

[f] *d-d* (Fe^{3+}) $^6A_{1g}(^6S)\rightarrow{}^4T_{1g}(^4P)$ contribution to the absorbance.

[g] The contribution to the absorbance of $t_{2u}^{\beta}\rightarrow t_{2g}^{\beta}$ LMCT transition is also present.

6.2. Ligand field analysis

The energy, expressed in cm^{-1}, of ligand field ($d\text{-}d$) transitions (*i.e.*, $\tilde{\nu}$) allows to calculate the ligand field splitting strength ($10Dq$), the Racah B and C parameters. In the octahedral (O_h) symmetry approximation, the equations describing the energy of $d\text{-}d$ transitions are the eigenvalues of Tanabe-Sugano matrices[30,31]. Nevertheless, in the iron case, several readily usable approximated equations are also available from literature[29,32]. Ligand field analysis results are summarized in **Table 5** in the main article.

6.2.1. Nickel

The Ni^{2+} ion has an $[Ar]4s^0 3d^8$ electronic configuration, resulting into five spin-orbit terms[33]. Two of these five terms are triplets, namely ^3F and ^3P, whereas the remaining three are singlets, namely ^1S, ^1D and ^1G (*cf.* **Diagram 1a** in the main article). According to Hund's rule[33], the spin-orbit term with the lowest energy is ^3F. In the O_h ligand field, the ^3F term is split into the singly degenerate $^3A_{2g}(^3F)$ ground state, the triply degenerate $^3T_{2g}(^3F)$ state and the triply degenerate $^3T_{1g}(^3F)$ state (**Diagram 1a**, violet lines). The former term represents the $(t_{2g}^{\alpha})^3(e_g^{\alpha})^2(t_{2g}^{\beta})^3$ ground configuration of electrons in Ni^{2+} ions' $3d$ orbitals, whereas the other two terms are generated by the $(t_{2g}^{\alpha})^3(e_g^{\alpha})^2(t_{2g}^{\beta})^2(e_g^{\beta})^1$ exited configuration[30,31]. The ^3P term represents the $(t_{2g}^{\alpha})^3(e_g^{\alpha})^2(t_{2g}^{\beta})^1(e_g^{\beta})^2$ exited configuration, which results from the promotion of two electrons from the t_{2g}^{β} to the e_g^{β} spin-orbitals[30,31]. In the O_h ligand field, the ^3P state only generates the triply degenerate $^3T_{1g}(^3P)$ state (**Diagram 1a**, cyan line). The $10Dq$ value of Ni^{2+} is straightforward from the energy of the first spin-allowed transition as follows[30,31,33]:

$$\tilde{\nu}\left[^3A_{2g}(^3F)\rightarrow{}^3T_{2g}(^3F)\right] = 10Dq \ .\#(S12)$$

The Racah B parameter proceeds from the energy of the second and third spin-allowed transitions by resolving the following equation respect to $\tilde{\nu}$ [30,31]

$$\det\left[\tilde{\nu}I_2 - T\left(^3A_{2g}(^3F)\rightarrow{}^3T_{1g}(^3F,{}^3P)\right)\right] = 0 \ \#(S13a)$$

$$-\begin{vmatrix} 3B + 20Dq - \tilde{\nu} & 6B \\ 6B & 12B + 10Dq - \tilde{\nu} \end{vmatrix} = 0 \ \#(S13b)$$

in which $T\left(^3A_2\rightarrow{}^3T_1\right)$ is the 2-by-2 matrix, representing transitions from the ground state to exited states with the $^3T_1$ symmetry term. I_n represents an n-by-n identity matrix ($n = 2$ in this case). The matrix in $(S13a)$ is built according to the table of matrix elements of Coulomb interactions related to $^3T_1$ states in d^2 electronic configurations[31] (d^{10-n} is complementary to d^n). Then, the energy difference compared to the $^3A_{2g}(^3F)$ ground state is subtracted from the diagonal elements (*cf.* also section 6.3.3). By solving $(S13b)$ with respect to $\tilde{\nu}$ the energy expressions describing the second and third spin-allowed transitions are obtained[30,31,33], namely:

$$\tilde{\nu}\left[^3A_{2g}(^3F)\rightarrow{}^3T_{1g}(^3F)\right] = \frac{15}{2}B + 15Dq - \sigma \#(S14a)$$

and

$$\tilde{\nu}\left[^3A_{2g}(^3F)\rightarrow{}^3T_{1g}(^3P)\right] = \frac{15}{2}B + 15Dq + \sigma \ ,\#(S14b)$$

where

$$\sigma = \frac{1}{2}\sqrt{(15B)^2 + (10Dq)^2 - 180BDq} \ .\#(S14c)$$

Analogously, the Racah C parameter proceeds from the energy of spin-forbidden transitions according to the following equations[30,31]:

$$\det\left[\tilde{\nu}I_2 - T\left({}^3A_{2g}\left({}^3F\right)\rightarrow{}^1E_g\left({}^1D,{}^1G\right)\right)\right] = -\begin{vmatrix} 9B+2C+20Dq-\tilde{\nu} & -2\sqrt{3}B \\ -2\sqrt{3}B & 8B+2C-\tilde{\nu}\end{vmatrix} = 0 \#(S15a)$$

$$\det\left[\tilde{\nu}I_2 - T\left({}^3A_{2g}\left({}^3F\right)\rightarrow{}^1A_{1g}\left({}^1G,{}^1S\right)\right)\right] = -\begin{vmatrix} 18B+5C+20Dq-\tilde{\nu} & \sqrt{6}(2B+C) \\ \sqrt{6}(2B+C) & 16B+4C-\tilde{\nu}\end{vmatrix} = 0 \#(S15b)$$

$$\det\left[\tilde{\nu}I_2 - T\left({}^3A_{2g}\left({}^3F\right)\rightarrow{}^1T_{2g}\left({}^1D,{}^1G\right)\right)\right] = -\begin{vmatrix} 9B+2C+20Dq-\tilde{\nu} & 2\sqrt{3}B \\ 2\sqrt{3}B & 8B+2C+10Dq-\tilde{\nu}\end{vmatrix} = 0 .\#(S15c)$$

Here, $(S15)$ equations yield the energies related to the energy of transitions to ${}^1E$, ${}^1A_1$ and ${}^1T_2$ states. The solutions of $(S15)$ with respect to $\tilde{\nu}$, which are relevant to our case, are the ones having the negative sign before the square root term, namely:

$$\tilde{\nu}\left[{}^3A_{2g}\left({}^3F\right)\rightarrow{}^1E_g\left({}^1D\right)\right] = \frac{17}{2}B + 2C + 10Dq - \frac{1}{2}\sqrt{(7B)^2 + (20Dq)^2 + 40BDq}\ ,\#(S16a)$$

$$\tilde{\nu}\left[{}^3A_{2g}\left({}^3F\right)\rightarrow{}^1A_{1g}\left({}^1G\right)\right] = 17B + \frac{9}{2}C + 10Dq - \frac{1}{2}\sqrt{(10B)^2 + (5C)^2 + (20Dq)^2 + 100BC + 80BDq + 40CDq}\#(S16b)$$

and

$$\tilde{\nu}\left[{}^3A_{2g}\left({}^3F\right)\rightarrow{}^1T_{2g}\left({}^1D\right)\right] = \frac{17}{2}B + 2C + 15Dq - \frac{1}{2}\sqrt{(7B)^2 + (10Dq)^2 + 20BDq}\ .\#(S16c)$$

Therefore, $10Dq$ was directly calculated from $\tilde{\nu}_1$ according to $(S12)$. Then B was calculated by combining $(S14)$ equations as follows:

$$B = \frac{\tilde{\nu}_{2,3} + \tilde{\nu}_5 - 30Dq}{15}.\#(S17)$$

We point out that, for B and C calculations, we decided to use the average value of $\tilde{\nu}_{2,3}$, instead of $\tilde{\nu}_2$ or $\tilde{\nu}_3$, due to spin-orbit coupling (*cf.* the main text). We reached this decision since, without averaging $\tilde{\nu}_2$ and $\tilde{\nu}_3$, the values of C obtained from $(S16a)$ were not consistent with the C yielded by $(S16b)$ and $(S16c)$. Our calculations yield $10Dq$ values of Ni^{2+} as 9,009 and 8,929 cm^{-1} for NiAl- and NiFe-LDH, respectively, while Racah parameter B values are 892 and 887 cm^{-1} for NiAl- and NiFe-LDH, respectively. It follows that Dq/B ratios are 1.01 for both NiAl- and NiFe-LDHs. By comparison, A. Harvey et al.[24] reported a $10Dq$ of exfoliated β-$Ni(OH)_2$ of 9,100 cm^{-1} and a B value of 830 cm^{-1}, resulting into a Dq/B ratio of 1.10. Eventually, we report that the values of C calculated according $(S16b)$ are 4,045 and 4,075 cm^{-1} for NiAl- and NiFe-LDH, respectively. This corresponds to C/B ratios of 4.50 for the NiAl-LDH and 4.59 NiFe-LDH. The same C values calculated according to $(S16a)$ resulted ~200 cm^{-1} lower, while C calculated according $(S16c)$ were ~200 cm^{-1} higher in comparison to values reported above.

6.2.2. Iron

The Fe^{3+} ion has an $[Ar]4s^0 3d^5$ electronic configuration, resulting into a total of 16 spin-orbit terms[33]. More precisely, 11 doublet terms, four quartet terms and one sextet term[33]. However, since we are limited only to high-spin electronic configurations, the relevant spin-orbit terms to consider are only the sextet ${}^6S$ term and the quartet ${}^4P$, ${}^4D$, ${}^4F$ and ${}^4G$ terms (*cf.* **Diagram 1b**). According to Hund's rule[33], the ${}^6S$ term is the one with the lowest energy. In the O_h ligand field, the ${}^6S$ term generates the singly degenerate ${}^6A_{1g}\left({}^6S\right)$ ground state (black line on the abscissae in **Diagram 1b**), which is representative of the $\left(t_{2g}^{\alpha}\right)^3\left(e_g^{\alpha}\right)^2$ ground configuration of electrons in Fe^{3+} $3d$ orbitals. Moreover, since in the ${}^6A_{1g}\left({}^6S\right)$ state all t_{2g} and e_g orbitals are half full of electrons all of which are in *α*-states, all possible d-d transitions are spin-forbidden. The first two Fe^{3+} excited states are the triply degenerate ${}^4T_{1g}\left({}^4G\right)$ and ${}^4T_{2g}\left({}^4G\right)$ states. They are representative of the

$\left(t_{2g}^{\alpha}\right)^3\left(e_g^{\alpha}\right)^1\left(t_{2g}^{\beta}\right)^1$ configuration, which arises from the electron pairing of one electron originating from the e_g^{α} spin-orbitals to the t_{2g}^{β} spin-orbitals[28,29]. The five ${}^4E_g\left({}^4G\right)$, ${}^4E,{}^4T_{2g}\left({}^4D\right)$ and ${}^4T_{1g}\left({}^4P\right)$ ligand field states are representative of two "spin-flip" configurations in the Fe^{3+} ion[28,29], namely $\left(t_{2g}^{\alpha}\right)^2\left(e_g^{\alpha}\right)^2\left(t_{2g}^{\beta}\right)^1$ and $\left(t_{2g}^{\alpha}\right)^3\left(e_g^{\alpha}\right)^1\left(e_g^{\beta}\right)^1$, whereas the ${}^4A_{1g}\left({}^4G\right)$ arises from the spin canting of e_g orbitals with respect to t_{2g} orbitals.

The energy of $d\text{-}d$ transitions in high-spin Fe^{3+} ions (in NiFe-LDH) are determined as follows.

$$\det\left[\tilde{\nu}I_3 - T\left({}^6A_1 \rightarrow {}^4T_1\right)\right] = -\begin{vmatrix} 10B+6C-10Dq-\tilde{\nu} & 3\sqrt{2}B & -C \\ 3\sqrt{2}B & 19B+7C-\tilde{\nu} & -3\sqrt{2}B \\ -C & -3\sqrt{2}B & 10B+6C+10Dq-\tilde{\nu} \end{vmatrix} = 0 \#(S18a)$$

$$\det\left[\tilde{\nu}I_3 - T\left({}^6A_1 \rightarrow {}^4T_2\right)\right] = -\begin{vmatrix} 18B+6C-10Dq-\tilde{\nu} & -\sqrt{6}B & -4B-C \\ -\sqrt{6}B & 13B+5C-\tilde{\nu} & -\sqrt{6}B \\ -4B-C & -\sqrt{6}B & 18B+6C+10Dq-\tilde{\nu} \end{vmatrix} = 0 \#(S18b)$$

$$\det\left[\tilde{\nu}I_2 - T\left({}^6A_1 \rightarrow {}^4E\right)\right] = -\begin{vmatrix} 13B+5C-\tilde{\nu} & -3\sqrt{2}B \\ -3\sqrt{2}B & 14B+5C-\tilde{\nu} \end{vmatrix} = 0 \#(S18c)$$

Here $(S18a)$ and $(S18b)$ yield the energies related to the energy of transitions to ${}^4T_1$ and ${}^4T_2$ states, respectively. For the sake of simplicity, we do not explicit the solutions to $(S18a)$ and $(S18b)$. The solutions to $(S18c)$ provide the energy of transitions to ${}^4E$ states, namely:

$$\tilde{\nu}\left[{}^6A_{1g}\left({}^6S\right) \rightarrow {}^4E_g\left({}^4G\right)\right] = 10B + 5C \#(S19a)$$

$$\tilde{\nu}\left[{}^6A_{1g}\left({}^6S\right) \rightarrow {}^4E_g\left({}^4D\right)\right] = 17B + 5C \#(S19b)$$

Transitions to ${}^4A_1$ and ${}^4A_2$ states are straightforward from their respective 1-by-1 matrices:

$$\tilde{\nu}\left[{}^6A_{1g}\left({}^6S\right) \rightarrow {}^4A_{1g}\left({}^4G\right)\right] = 10B + 5C \#(S20a)$$

$$\tilde{\nu}\left[{}^6A_{1g}\left({}^6S\right) \rightarrow {}^4A_{2g}\left({}^4F\right)\right] = 22B + 7C \#(S20b)$$

According to our band assignments (*cf.* **Table 4** in the main text), the Racah B and C parameters of Fe^{3+} can be obtained from the energy of $\tilde{\nu}_4$ and $\tilde{\nu}_7$ according to $(S19a)$ and $(S19b)$, respectively. More in detail, our calculations yielded values of Fe^{3+} Racah B and C parameters equal to 916 and 2,632 cm^{-1}, respectively.

6.2.3. Computing Tanabe-Sugano diagrams with MATLAB

In this section, we describe the computing procedure of Tanabe-Sugano diagrams reported in the main text (**Diagram 1**). To perform these computation tasks, we used our homebuilt MATLAB app which can compute Tanabe-Sugano diagrams with custom values of C/B ratio[34]. Here we report the procedure specific to high-spin Fe^{3+} as an example. However, diagrams describing other transition-metal ions can be derived by following analogous procedures.

6.2.3.1 Computation of matrices and eigenvalues.

In MATLAB energy matrices are expressed symbolically. At first, symbolic elements B, C and Δ_0 ($\Delta_0 = 10Dq$) are defined by the `syms` function. Then, matrices of Coulomb interactions are built from their respective tables of matrix elements[30,31]. The matrices of Coulomb interactions are grouped into a cell arrays to vectorize computations. Here, the Coulomb interactions matrix of ${}^4T_1$ states is brought as an example:

$$A\left({}^4T_1\right) = \begin{pmatrix} -25B+6C & 3\sqrt{2}\cdot B & -C \\ 3\sqrt{2}\cdot B & -16B+7C & -3\sqrt{2}\cdot B \\ -C & -3\sqrt{2}\cdot B & -25B+6C \end{pmatrix} .\#(S21)$$

Energy matrices describing ligand field states are computed by adding to each matrix of Coulomb interactions its corresponding diagonal matrix of electronic configuration energies[31]. More in detail, the energy term of a $t_2^n e^m$ electronic configuration is defined as:

$$E = \frac{\Delta_0}{10} \cdot (6m - 4n) \ ,\#(S22a)$$

whereas the energy term of its complementary configuration, namely $t_2^{6-n} e^{4-m}$, is defined as:

$$E = \frac{\Delta_0}{10} \cdot (4n - 6m) \ .\#(S22b)$$

In Fe^{3+} case, the configurations energy terms are defined according to $t_2^n e^m$ electronic configurations reported in the header lines of d^5 tables of matrix elements[30,31]. Here, the energy matrix is of $^4T_1$ states is brought as an example:

$$E(^4T_1) = A(^4T_1) + \frac{\Delta_0}{10} \cdot diag(-10, 0, 10) = \begin{pmatrix} -25B + 6C - \Delta_0 & 3\sqrt{2} \cdot B & -C \\ 3\sqrt{2} \cdot B & -16B + 7C & -3\sqrt{2} \cdot B \\ -C & -3\sqrt{2} \cdot B & -25B + 6C + \Delta_0 \end{pmatrix} .\#(S23)$$

Tanabe-Sugano matrices are computed by subtracting the energy of the ground state from the diagonal elements of energy matrices. In the high-spin Fe^{3+} case, the energy of the ground state is:

$$E(^6A_1) = -35B \ .\#(S24)$$

Here, the matrix of $^6A_1(^6S) \rightarrow {}^4T_1$ transitions is brought as an example:

$$T(^6A_1 \rightarrow {}^4T_1) = E(^4T_1) - E(^6A_1) \cdot I_3 = \begin{pmatrix} 10B + 6C - \Delta_0 & 3\sqrt{2} \cdot B & -C \\ 3\sqrt{2} \cdot B & 19B + 7C & -3\sqrt{2} \cdot B \\ -C & -3\sqrt{2} \cdot B & 10B + 6C + \Delta_0 \end{pmatrix} ,\#(S25)$$

where I_3 is the 3-by-3 identity matrix. The equation describing the energy of electronic transition are the eigenvalues of Tanabe-Sugano matrices. For example:

$$eig\left(T(^6A_1 \rightarrow {}^4T_1)\right) = \begin{pmatrix} \tilde{\nu}[^6A_1(^6S) \rightarrow {}^4T_1(^4G)] \\ \tilde{\nu}[^6A_1(^6S) \rightarrow {}^4T_1(^4P)] \\ \tilde{\nu}[^6A_1(^6S) \rightarrow {}^4T_1(^4F)] \end{pmatrix} ,\#(S26)$$

which is equivalent to solving $(S18a)$**.** The diagrams are obtained by computing the numerical values of all eigenvalues, at a fixed B/C ratio, across an array of Δ_0 values*.

6.2.3.2 Ligand field parameters computation from experimental data.

The procedure for computing Fe^{3+} ligand field parameters is reported in the example code below. To perform this task, at least three non-degenerate electronic transitions are required. More in detail, in the high-spin Fe^{3+} case we used the energy values of the $^6A_{1g}(^4S) \rightarrow {}^4A_1, {}^4E(^4G)$ transition, the $^6A_{1g}(^4S) \rightarrow {}^4E(^4D)$ transition and the $^6A_{1g}(^4S) \rightarrow {}^4T_1(^4P)$ transition, which fall at 448, 348 and 338 nm, respectively. For the sake of clarity, in the code these energies are referred to as `nu1`, `nu2` and `nu3` variables (not to be confused with ν_1, ν_2 and ν_3). The equations `eq_4E(1,1)`, `eq_4E(2,1)` and `eq_4T1(2,1)` are provided by our MATLAB app[34]. Then, the ligand field parameters are obtained by solving a system of the three equations representing the aforementioned energy transitions. In this case, two opposite solutions are returned, since `eq_4T1(2,1)` is a 2nd degree equation with respect to Δ_0.

```
% Insert the energy in (cm^{-1}) of three non-degenerate electronic transitions.
```

* MATLAB is able to algebraically compute eigenvalues up to the 4th degree, while 5th degree or greater eigenvalues are expressed via the `root(_)` function.

```
nu1 = 1e7/448;
nu2 = 1e7/348;
nu3 = 1e7/338;

% Assign the energy of each transition with the corresponding equation exported from the app.
state1 = eq_4E(1,1);
state2 = eq_4E(2,1);
state3 = eq_4T1(2,1);

% Define the free-ion Racah parameters.
B0 = 1015;
C0 = 4800;

% Build and solve a 3-by-3 system of equations.
eq1 = state1 == nu1; % 1st equation
eq2 = state2 == nu2; % 2nd equation
eq3 = state3 == nu3; % 3rd equation
eqns = [eq1,eq2,eq3]; % System of equations
S = solve(eqns,[Delta_0 B C]); % Solve the system

% Store results into a table.
% Note: the system has two different solutions. Discard the one with negative Delta_0.
results = table;
results.Delta_0 = double(S.Delta_0);
results.B = double(S.B);
results.C = double(S.C);
results.field = results.Delta_0./results.B;
results.gamma = results.C./results.B;
results.beta = results.B./B0;
results.beta1 = sqrt((results.B./B0).^2+(results.C./C0).^2);
display(results) % Display the results.
```

results = 2×7 table

	Delta_0	B	C	field	gamma	beta	beta1
1	-7.0493e+03	916.3148	2.6317e+03	-7.6931	2.8720	0.9028	1.0562
2	7.0493e+03	916.3148	2.6317e+03	7.6931	2.8720	0.9028	1.0562

7. References

(1) Tichit, D.; Layrac, G.; Alvarez, M. G.; Marcu, I. C. Formation Pathways of MII/MIII Layered Double Hydroxides: A Review. *Applied Clay Science*. Elsevier Ltd February 1, 2024. https://doi.org/10.1016/j.clay.2023.107234.

(2) Jaśkaniec, S.; Hobbs, C.; Seral-Ascaso, A.; Coelho, J.; Browne, M. P.; Tyndall, D.; Sasaki, T.; Nicolosi, V. Low-Temperature Synthesis and Investigation into the Formation Mechanism of High Quality Ni-Fe Layered Double Hydroxides Hexagonal Platelets. *Sci Rep* **2018**, *8* (1), 4–11. https://doi.org/10.1038/s41598-018-22630-0.

(3) Piccinni, M.; Bellani, S.; Bianca, G.; Bonaccorso, F. Nickel–Iron Layered Double Hydroxide Dispersions in Ethanol Stabilized by Acetate Anions. *Inorg Chem* **2022**, *61* (11), 4598–4608. https://doi.org/10.1021/acs.inorgchem.1c03485.

(4) Tronto, J.; dos Reis, M. J.; Silvério, F.; Balbo, V. R.; Marchetti, J. M.; Valim, J. B. In Vitro Release of Citrate Anions Intercalated in Magnesium Aluminium Layered Double Hydroxides. *Journal of Physics and Chemistry of Solids* **2004**, *65* (2–3), 475–480. https://doi.org/10.1016/j.jpcs.2003.09.019.

(5) Zhang, J.; Zhang, F.; Ren, L.; Evans, D. G.; Duan, X. Synthesis of Layered Double Hydroxide Anionic Clays Intercalated by Carboxylate Anions. *Mater Chem Phys* **2004**, *85* (1), 207–214. https://doi.org/10.1016/j.matchemphys.2004.01.020.

(6) Meyn, M.; Beneke, K.; Lagaly, G. Anion-Exchange Reactions of Layered Double Hydroxides. *Inorg Chem* **1990**, *29* (26), 5201–5207. https://doi.org/10.1021/ic00351a013.

(7) Oliver-Tolentino, M. A.; Vázquez-Samperio, J.; Manzo-Robledo, A.; González-Huerta, R. D. G.; Flores-Moreno, J. L.; Ramírez-Rosales, D.; Guzmán-Vargas, A. An Approach to Understanding the Electrocatalytic Activity Enhancement by Superexchange Interaction toward OER in Alkaline Media of Ni-Fe LDH. *Journal of Physical Chemistry C* **2014**, *118* (39), 22432–22438. https://doi.org/10.1021/jp506946b.

(8) Coronado, E.; Galén-Mascarós, J. R.; Martí-Gastaldo, C.; Ribera, A.; Palacios, E.; Castro, M.; Burriel, R. Spontaneous Magnetization in Ni-Al and Ni-Fe Layered Double Hydroxides. *Inorg Chem* **2008**, *47* (19), 9103–9110. https://doi.org/10.1021/ic801123v.

(9) Mills, S. J.; Christy, A. G.; Génin, J.-M. R.; Kameda, T.; Colombo, F. Nomenclature of the Hydrotalcite Supergroup: Natural Layered Double Hydroxides. *Mineral Mag* **2012**, *76* (5), 1289–1336. https://doi.org/10.1180/minmag.2012.076.5.10.

(10) Alderighi, L.; Gans, P.; Ienco, A.; Peters, D.; Sabatini, A.; Vacca, A. Hyperquad Simulation and Speciation (HySS): A Utility Program for the Investigation of Equilibria Involving Soluble and Partially Soluble Species. *Coord Chem Rev* **1999**, *184* (1), 311–318. https://doi.org/10.1016/S0010-8545(98)00260-4.

(11) Donald R. Burgess. *Critically Selected Stability Constants of Metal Complexes: Version 8.0 for Windows, National Institute of Standards and Technology*. https://doi.org/https://doi.org/10.18434/M32154.

(12) Silva, A. M. N.; Kong, X.; Parkin, M. C.; Cammack, R.; Hider, R. C. Iron(III) Citrate Speciation in Aqueous Solution. *Dalton Transactions* **2009**, No. 40, 8616–8625. https://doi.org/10.1039/b910970f.

(13) Mech, K. Influence of Organic Ligands on Electrodeposition and Surface Properties of Nickel Films. *Surf Coat Technol* **2017**, *315*, 232–239. https://doi.org/10.1016/j.surfcoat.2017.02.042.

(14) Plyasunova, N. V; Zhang, Y.; Muhammed, M. *Critical Evaluation of Thermodynamics of Complex Formation of Metal Ions in Aqueous Solutions. IV. Hydrolysis and Hydroxo-Complexes of Ni 2q at 298.15 K*; 1998; Vol. 48.

(15) Konig, E.; Hemmerich, P.; Jorgensen, C. K.; Neilands, J. B.; Nybolm, R. S.; Reinen, D.; Williams, R. J. P. The Nephelauxetic Effect. *Struct Bond* **1971**, *9*, 175–212.

(16) Still, E. R.; Wikberg, P. Solution Studies of Systems with Polynuclear Complex Formation. 2. The Nickel(II) Citrate System. *Inorganica Chim Acta* **1980**, *46* (C), 153–155. https://doi.org/10.1016/S0020-1693(00)84184-5.

(17) Timberlake, C. F. 975. Iron–Malate and Iron–Citrate Complexes. *J. Chem. Soc.* **1964**, *0* (0), 5078–5085. https://doi.org/10.1039/JR9640005078.

(18) Gregor, J.; Powell, H. Aluminum(III)-Citrate Complexes: A Potentiometric and 13C N.M.R.-Study. *Aust J Chem* **1986**, *39* (11), 1851. https://doi.org/10.1071/CH9861851.

(19) Silva, A. M. N.; Kong, X.; Hider, R. C. Determination of the PKa Value of the Hydroxyl Group in the α-Hydroxycarboxylates Citrate, Malate and Lactate by 13C NMR: Implications for Metal Coordination in Biological Systems. *BioMetals* **2009**, *22* (5), 771–778. https://doi.org/10.1007/s10534-009-9224-5.

(20) Capone, S.; De Robertis, A.; De Stefano, C.; Sammartano, S. Formation and Stability of Zinc(II) and Cadmium(II) Citrate Complexes in Aqueous Solution at Various Temperatures. *Talanta* **1986**, *33* (9), 763–767. https://doi.org/10.1016/0039-9140(86)80184-9.

(21) Daniele, P. G.; Ostacoli, G. MIXED COMPLEX FORMATION OF ZN2+ ION AND CITRIC ACID WITH L-HISTIDINE OR HISTAMINE IN AQUEOUS SOLUTION. *ANN. CHIM.; ITAL.* **1977**, *67* (1–2), 37–49.

(22) Rudolf, C.; Dragoi, B.; Ungureanu, A.; Chirieac, A.; Royer, S.; Nastro, A.; Dumitriu, E. NiAl and CoAl Materials Derived from Takovite-like LDHs and Related Structures as Efficient Chemoselective Hydrogenation Catalysts. *Catal Sci Technol* **2014**, *4* (1), 179–189. https://doi.org/10.1039/c3cy00611e.

(23) Scheinost, A. C.; Ford, R. G.; Sparks, D. L. The Role of Al in the Formation of Secondary Ni Precipitates on Pyrophyllite, Gibbsite, Talc, and Amorphous Silica: A DRS Study. *Geochim Cosmochim Acta* **1999**, *63* (19–20), 3193–3203. https://doi.org/10.1016/S0016-7037(99)00244-6.

(24) Harvey, A.; He, X.; Godwin, I. J.; Backes, C.; McAteer, D.; Berner, N. C.; McEvoy, N.; Ferguson, A.; Shmeliov, A.; Lyons, M. E. G.; Nicolosi, V.; Duesberg, G. S.; Donegan, J. F.; Coleman, J. N. Production of Ni(OH)2 Nanosheets by Liquid Phase Exfoliation: From Optical Properties to Electrochemical Applications. *J Mater Chem A Mater* **2016**, *4* (28), 11046–11059. https://doi.org/10.1039/c6ta02811j.

(25) Poul, L.; Jouini, N.; Fievet, F. Layered Hydroxide Metal Acetates (Metal = Zinc, Cobalt, and Nickel): Elaboration via Hydrolysis in Polyol Medium and Comparative Study. *Chemistry of Materials* **2000**, *12* (10), 3123–3132. https://doi.org/10.1021/cm991179j.

(26) Qi, Y.; Qi, H.; Li, J.; Lu, C. Synthesis, Microstructures and UV-Vis Absorption Properties of β-Ni(OH)2 Nanoplates and NiO Nanostructures. *J Cryst Growth* **2008**, *310* (18), 4221–4225. https://doi.org/10.1016/j.jcrysgro.2008.06.047.

(27) de Moura, A. P.; Lima, R. C.; Paris, E. C.; Li, M. S.; Varela, J. A.; Longo, E. Formation of β-Nickel Hydroxide Plate-like Structures under Mild Conditions and Their Optical Properties. *J Solid State Chem* **2011**, *184* (10), 2818–2823. https://doi.org/10.1016/j.jssc.2011.08.027.

(28) Sherman, D. M. The Electronic Structures of Fe3+ Coordination Sites in Iron Oxides: Applications to Spectra, Bonding, and Magnetism. *Phys Chem Miner* **1985**, *12* (3), 161–175. https://doi.org/10.1007/BF00308210.

(29) Sherman, D. M.; Waite, T. D. Electronic Spectra of Fe3+ Oxides and Oxide Hydroxides in the near IR to near UV. *American Mineralogist* **1985**, *70* (11–12), 1262–1269.

(30) Tanabe, Y.; Sugano, S. On the Absorption Spectra of Complex Ions. I. *J Physical Soc Japan* **1954**, *9* (5), 753–766. https://doi.org/10.1143/JPSJ.9.753.

(31) Sugano, S.; Tanabe, Y.; Kamimura, H. Pure and Applied Physics: A Series of Monographs and Textbooks. In *Pure and applied physics v. 33.*; 1970; Vol. 33, pp 332–333. https://doi.org/10.1016/b978-0-12-676050-7.50027-5.

(32) Jørgensen, Chr. K. Spectroscopy of Transition-Group Complexes; 2007; pp 33–146. https://doi.org/10.1002/9780470143513.ch2.

(33) Huheey, J. E.; Keiter, E. A.; Keiter, R. L. *Inorganic Chemistry: Principles of Structure and Reactivity*; Pearson College Div, 1993.

(34) Marco Piccinni. *Tanabe-Sugano diagrams with MATLAB*. MATLAB Central File Exchange. https://www.mathworks.com/matlabcentral/fileexchange/117420-tanabe-sugano-diagrams (accessed 2022-09-12).